FOCUS ISSUE

HETEROGENEITY IN 2D MATERIALS

Functionalization of single-layer TaS$_2$ and formation of ultrathin Janus structures

Zeynep Kahraman[1,a)], Mehmet Yagmurcukardes[2], Hasan Sahin[1,b)]

[1]Department of Photonics, Izmir Institute of Technology, Izmir 35430, Turkey
[2]Department of Physics, University of Antwerp, Antwerpen B-2020, Belgium
a)Address all correspondence to these authors. e-mail: mehmetyagmurcukardes.edu@gmail.com
b)e-mail: hasansahin@iyte.edu.tr
This paper has been selected as an Invited Feature Paper.

Ab initio calculations are performed to investigate the structural, vibrational, electronic, and piezoelectric properties of functionalized single layers of TaS$_2$. We find that single-layer TaS$_2$ is a suitable host material for functionalization via fluorination and hydrogenation. The one-side fluorinated (FTaS$_2$) and hydrogenated (HTaS$_2$) single layers display indirect gap semiconducting behavior in contrast to bare metallic TaS$_2$. On the other hand, it is shown that as both surfaces of TaS$_2$ are saturated anti-symmetrically, the formed Janus structure is a dynamically stable metallic single layer. In addition, it is revealed that out-of-plane piezoelectricity is created in all anti-symmetric structures. Furthermore, the Janus-type single-layer has the highest specific heat capacity to which longitudinal and transverse acoustical phonon modes have contribution at low temperatures. Our findings indicate that single-layer TaS$_2$ is suitable for functionalization via H and F atoms that the formed, anti-symmetric structures display distinctive electronic, vibrational, and piezoelectric properties.

Introduction

Successful exfoliation of graphene from the graphite in 2004 has opened a new research field in materials science. Many novel two-dimensional (2D) materials such as h-BN, silicene, h-AlN, and transition metal chalcogenides (TMCs) have gained considerable interest because of their unique electronic, optical, and mechanical properties [1, 2, 3, 4, 5, 6, 7]. Among 2D materials, TMCs have been the focus of interest over the last decade in the fields of electronic devices, energy conservation, and storage owing to their electronic properties ranging from metallic and semiconductor behavior, tunable band gaps, and controllable electronic and high optoelectronic properties [8, 9, 10, 11, 12, 13, 14, 15, 16, 17, 18, 19, 20, 21, 22].

TaS$_2$ has attracted great attention and has been extensively investigated as an important member of TMCs because of its superconducting state. TaS$_2$ has four different phases over a wide temperature range, from 77 to 400 K [23, 24]. In its layered form, TaS$_2$ was reported to be the only TMCs possessing the Mott phase. In addition, the external effects such as atomic and electron doping were shown to manipulate properties of TaS$_2$ significantly. For instance, in a developed

ionic effect transistor, Li-ion interference has been reported to modulate the properties of TaS$_2$. Strong charge doping induced by adjustable ion intercalation changes the energy of the various charge sequence states in TaS$_2$ and produces a series of phase transitions in dimensionally reduced flake samples [25]. Moreover, high hydrogen evolution reaction efficiency was obtained for TaS$_2$, revealing its novelty and efficiency in catalysts [26].

Functionalization of 2D materials has been experimentally demonstrated that the properties of the ultrathin materials can be tuned controllably. It was shown that fluorination in 2D materials can lead to tunable electronic, optical, and mechanical properties [27, 28, 29, 30, 31]. Fluorinated graphene has been announced to be more efficient for oxygen reduction reaction (ORR) catalysts because of its lower overpotential and a good alternative to a metal-free catalyst for the removal of organic pollutants in catalytic ozonation [32, 33]. Hydrogenation is also an important and common process for chemical functionalization of 2D materials [34]. One or two-surface hydrogenated graphene structures were shown to exhibit tunable band gap depending on the atomic arrangements of H

atoms [35]. Chemical functionalization creates a tunable band gap in 2D materials, allowing for conductive, flexible, transparent device structures using the electronic, optical, and mechanical properties of the materials [36, 37, 38].

In addition to the research on 2D symmetric materials, Janus-type 2D materials were obtained, which allows the collection of different properties of ultrathin crystals in a single polar material [39, 40, 41, 42, 43, 44]. It was revealed that the intrinsic out-of-plane electric field induced in Janus structures cause giant Rashba spin splitting in the electronic band distribution and Janus structures exhibit enhanced piezoelectric properties [42, 43, 44].

In this study, we investigate the structural, vibrational, electronic, and piezoelectric properties of single-layer TaS_2 structures including its functionalized derivatives. The rest of this article is organized as follows: the details of the DFT calculations are given in the computational methodology section. The properties of the TaS2 structures are discussed in detail in the Results section. Finally, we conclude our results in the conclusion section

Results

Structure, stability, and electronic properties

Single-layer of TaS_2

The bulk forms of layered TaS_2 with trigonal $1T$–TaS_2 ($P6m1$), hexagonal $2H$–TaS_2 ($P6m3$), and rhombohedral $3R$–TaS_2 ($R3m$) phases have been widely investigated as the most common bulk phases. The optimized crystal structure of single-layer hexagonal $1H$–TaS_2 is shown in Fig. 1(a). TaS_2 has a hexagonal crystal structure consisting of Ta layer sandwiched between two S layers. The optimized in-plane lattice parameters ($a = b$) are found to be 3.36 Å and is compatible with the previously reported atomic-resolution Transmission Electron Microscopy (TEM) observations [26]. The bond length between Ta and S atoms is found to be 2.48 Å. Moreover, the thickness of single-layer TaS_2, distance between the upper and lower sides S layers, is found to be 3.11 Å. As listed in Table I, cohesive energy of TaS_2 is found to be 6.27 eV/atom, which is slightly larger than that of reported for single-layer MoS_2 (5.18 eV/atom) [51]. Bader charge analysis shows that each S atom receives 0.8 e^- from a Ta atom. The electronic properties of the single-layer TaS_2 is investigated through its electronic band dispersions and the corresponding partial density of states (PDOS) as shown in Fig. 1(c). Electronically, single-layer TaS_2 is found to possess a metallic character with the nonzero density of states at the Fermi level. In addition, the PDOS reveal that Ta-d orbitals dominate the bands crossing the Fermi level.
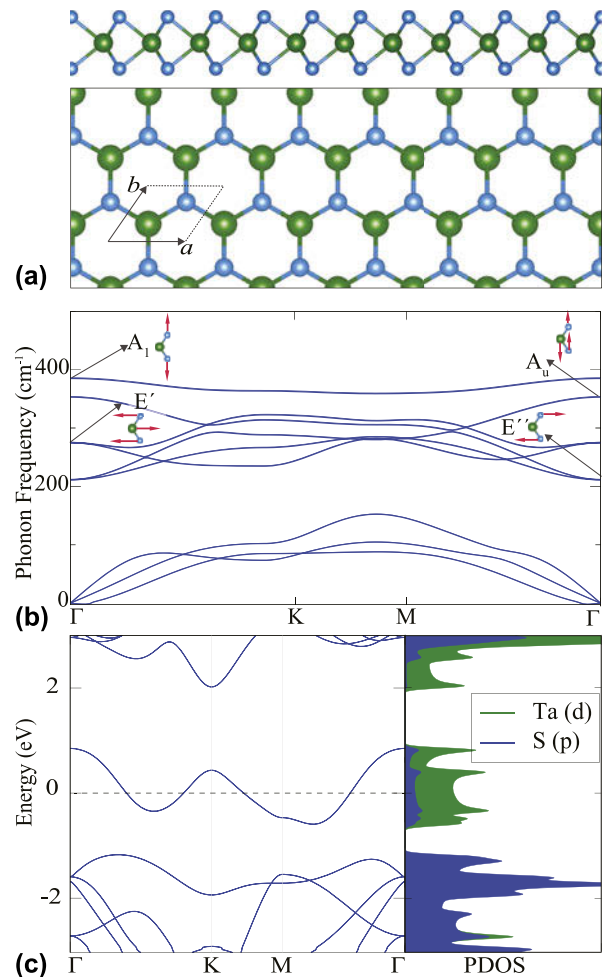

Figure 1: For single-layer TaS_2: (a) top and side views of the crystal structure. Green and blue colors represent Ta and S atoms, respectively. (b) Phonon band structure. The inset shows the vibrational character of the optical phonon modes at the Γ point. On the right panel, the corresponding Raman spectrum is shown. (c) The electronic band structure and the corresponding PDOS. The Fermi energy is set to 0 eV level.

The calculated phonon band dispersions of single-layer TaS_2 indicate its dynamical stability [see Fig. 1(b)]. Phonon band gap between the optical and acoustic phonon branches in single-layer TaS_2 is calculated to be 59 cm^{-1} slightly larger than that of single-layer MoS_2 (~46 cm^{-1}). The optical phonon branches of single-layer TaS_2 consist of two doubly degenerate in-plane modes having frequency 212 cm^{-1} (E'') and 275 cm^{-1} (E'), and two nondegenerate out-of-plane modes at 353 cm^{-1} (A_u) and 385 cm^{-1} (A_1) at the Γ point. The phonon modes A_1, E', and E'' are known as the Raman active modes whose Raman spectrum is given on the right panel of Fig. 1(b). The A_1 mode is attributed to the out-of-plane vibration of S atoms against each other, whereas E' represents their opposite in-plane vibrations. Moreover, the E'' mode originates from the opposite in-plane vibrations of Ta-layer and two S-layers against each other. Apparently, the E'' mode exhibits the lowest Raman

TABLE I: The calculated parameters for single-layers of TaS_2 structures, $FTaS_2$, $HTaS_2$, and Janus $HTaS_2F$ are: the lattice constants, $a = b$; the atomic distance between S and X atoms (X = F, H), d; the thickness of single-layer, h; the cohesive energy per atom, E_{Coh}; initial and final charges of Ta, S, F, and H atoms, ρ_{Ta}, ρ_S, ρ_F, ρ_H; net magnetic moment per primitive cell, μ; and the energy band gap of the structures calculated, E_{Gap}.

	$a = b$ (Å)	d_{Ta-S} (Å)	d_{S-F} (Å)	d_{S-H} (Å)	h (Å)	E_{Coh} (eV/atom)	ρ_{Ta} initial-final (e⁻)	ρ_S initial-final (e⁻)	ρ_F ini-fin (e⁻)	ρ_H ini-fin (e⁻)	μ μB	E_{Gap} (eV)
TaS_2	3.36	2.48	. . .	. . .	3.11	6.27	5.0–3.4	6.0–6.8	. . .	. . .	0	. . .
$FTaS_2$	3.43	2.41/2.51	1.65	. . .	4.55	5.38	5.0–3.6	6.0–6.7	7.0–7.6	. . .	0	0.65
$HTaS_2$	3.42	2.45/2.49	. . .	1.37	4.34	5.13	5.0–3.6	6.0–6.7	. . .	1.0–1.0	0	0.96
$HTaS_2F$	3.42	2.43/2.50	1.71	1.40	6.07	4.58	5.0–3.6	6.0–6.4	7.0–7.6	1.0–1.0	0	. . .

activity among the three Raman active modes which is the case for all H-phase TMDs.

One-side fluorinated TaS_2

The pioneering work of Nair et al. [27] has shown that fluorinated graphene has been formed by laying fluorine successfully on graphene experimentally. The fluorinated graphene structure was reported to be teflon-like, semiconductor, and also flexible material. In another theoretical study, it has been shown that the form and composition of fluorine atoms play an important role in the alteration of properties such as binding energies, band spacings, and phonon modes. Because of the electronic properties, the stable C_2F chair structure is metallic, whereas CF with nonmagnetic character is an insulator [28].

F with nonmagnetic character is an insulator [28]. Figure 2(a) shows the atomic structure of single-layer $FTaS_2$; $FTaS_2$ belongs to $P6m3$ space groups and has hexagonal Bravais lattice. As listed in Table I, the optimized lattice parameter of $FTaS_2$ is 3.43 Å, whereas the thickness of single-layer $FTaS_2$ is 4.55 Å with the corresponding Ta-S and S-F bond lengths of 2.41/2.51 and 1.65 Å, respectively. Bader charge analysis shows that each Ta atom donates 0.7 e⁻ to an F and 0.6 e⁻ to an S atom, respectively. For single-layer $FTaS_2$, the cohesive energy is calculated to be 5.38 eV/atom smaller than that of bare TaS_2. As shown in Fig. 2(c), the electronic band dispersion and electronic density of states reveal that single-layer $FTaS_2$ exhibits indirect band gap semiconducting behavior with a band gap of 0.65 eV. The valence band maximum (VBM) of single-layer $FTaS_2$ lies at the K point, whereas the conduction band minimum (CBM) resides between the Γ and the K points. Excitonic transitions shift because of indirect band gap from the K point. Moreover, it is shown that CBM state arises from localized S-p and F-p orbitals, whereas the VBM is dominated by Ta-d orbitals. In addition, occupation of p-orbitals of S atoms by F atoms results in shift of the bands around the Fermi level to low energies driving the metal-to-semiconductor transition.

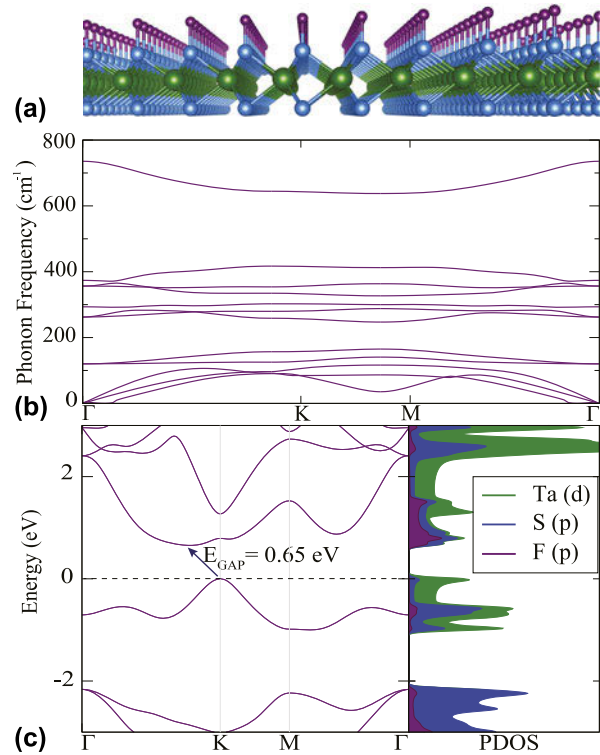Phonon band dispersions of single-layer $FTaS_2$ indicate its dynamical stability. As seen in Fig. 2(b), single-layer $FTaS_2$ has

Figure 2: (a) Perspective side view of $FTaS_2$. Green, blue, and purple colors show Ta, S, and F atoms, respectively. (b) Phonon band dispersions with the corresponding Raman spectrum (on the right) and (c) the electronic band dispersion with the corresponding PDOS for single-layer $FTaS_2$. The Fermi level energy is set to 0 eV.

twelve phonon branches, three of which are acoustic and the remaining nine are optical phonon branches. The acoustic–optical phonon band gap (19 cm⁻¹) is found to be lower than that of the bare structure. Single-layer $FTaS_2$ structure consists of three in-plane doubly degenerate and three out-of-plane nondegenerate phonon modes. The in-plane phonon mode at frequency 119 cm⁻¹ represents the opposite vibration of F atom and Ta–S pair in which the S atom is at the lower plane. The phonon mode has a similar vibrational character to E' mode in symmetric TaS_2. The other doubly degenerate phonon modes are calculated to have frequencies 262 and 355 cm⁻¹. The mode at 262 cm⁻¹ is attributed to the Ta–S and F–S pairs against each other that the F and the lower S atoms vibrate in-phase. Apparently, the mode has similar vibrational behavior to

the E_u mode in single-layer TaS_2. The in-plane phonon mode at frequency 355 cm^{-1} shows the opposite vibration of each atomic layer against each other that the F and Ta layers vibrate in-phase, whereas the two S layers vibrate oppositely to F–Ta layers. Apart from the in-plane phonon modes, the three out-of-plane phonon modes are calculated to have frequencies 290, 374, and 736 cm^{-1}, respectively. The lowest frequency out-of-plane mode reveals the opposite vibration of F layer against the TaS_2 layer that the two S layers and the Ta layers vibrate in-phase. Another nondegenerate mode having frequency 374 cm^{-1} represents vibration of Ta layer against the F–S–S layers. It can be related to the A_{2u} phonon mode of single-layer TaS_2. Finally, the highest frequency nondegenerate phonon mode consists of the opposite vibration of F and top-S layers against each other. The calculated Raman spectrum [see right panel of Fig. 2(b)] reveals that all the phonon modes are Raman active, except for the doubly degenerate optical mode at 119 cm^{-1} in which the atomic motion is not symmetric. Notably, adsorption of F atoms on one surface of single-layer TaS_2 results in distinctive vibrational spectrum of the anti-symmetric single-layer $FTaS_2$.

One-side hydrogenated TaS_2

It is an important method to use the chemical functionality to adjust the structural, electronic, and magnetic properties of 2D materials. In a study by Elias et al. [53], it was shown that highly conductive graphene can be converted into an insulator by hydrogenating the surface of graphene. In another theoretical study, it was shown that a band gap that can be defined in $TiSe_2$ is opened via hydrogenation [54].

The optimized atomic structure of single-layer $HTaS_2$ is shown in Fig. 3(a). Single-layer $HTaS_2$ resembles the hexagonal structure of single-layer TaS_2 with Bravais lattice vectors, $a = 0.5a(\sqrt{3}x - y)$, $b = 0.5a(\sqrt{3}x + y)$, and $c = c\,z$. As shown in Table I, optimized lattice parameters are $a = b = 3.42$ Å. The bond lengths between Ta atom and S atom are found to be 2.45/2.49 Å, whereas that of H–S is 1.37 Å [7]. The optimized structure is formed with a cohesive energy of 5.13 eV/atom, which is lower than that of $FTaS_2$ in accordance with the lower electronegativity of H atom than that of F. According to the Bader charge analysis, there is a charge depletion of 1.4 e$^-$ from Ta atom to S atom, whereas there is no charge transfer between H atom and the other atoms. Figure 3(c) shows the electronic band dispersions and corresponding partial density of states of single-layer $HTaS_2$. Single-layer $HTaS_2$ is a semiconductor, with VBM lying at the M point and the CBM residing between the M and the Γ points, and exhibiting an indirect band gap of 0.96 eV. It is found from the calculated PDOS that VBM states are mainly composed of the Ta-d orbitals and the S-p orbitals, whereas in the vicinity of
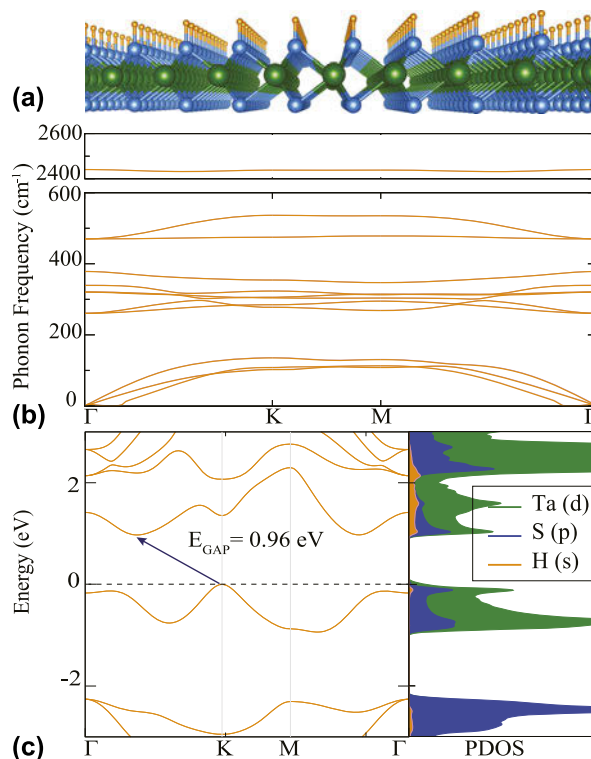

Figure 3: (a) Perspective side view of $HTaS_2$. Green, blue, and orange colors denote Ta, S, and H atoms, respectively. (b) Phonon band dispersions of $HTaS_2$, and Raman spectrum of the Raman active modes (on the right). (c) The electronic band structure and PDOS. The Fermi level energy is set to 0 eV.

CBM states, there is also the H-s orbital contribution in addition to the S-p and Ta-d orbitals. Similar to the case of single-side fluorinated structure, the bands around the Fermi level display a shift to lower energies and result in semiconducting behavior for $HTaS_2$. Figure 3(b) shows the phonon band structure of $HTaS_2$ which indicate the dynamical stability of the structure. Similarly, single-layer $HTaS_2$ possesses nine optical phonon branches. There is a huge gap between acoustic and optic phonon branches, 126 cm^{-1}, as compared with bare and $FTaS_2$ structures. The larger phonon band gap of $HTaS_2$ reveals its relatively high phonon transport properties. Because the adsorption sites of H atoms are the same as that of F atoms, the vibrational motion of the atoms are also similar to each other. However, the frequencies of the modes are not similar because of the changes in structural parameters. In single-layer $HTaS_2$, the lowest frequency in-plane phonon mode is found to be at 261 cm^{-1}. In the phonon mode, two S layers vibrate out-of-phase of each other, whereas the H atoms vibrate in-phase with the top-S layer where the Ta layer has no contribution to the vibration. The vibrational character of the mode at 321 cm^{-1} is determined by the opposite vibrations of lower-S and F-top-S layers against Ta layer. Vibration of the atoms in the phonon mode is similar to the E' of single-layer TaS_2 with an anti-symmetric vibration with respect to the Ta layer. In

addition, the other doubly degenerate at 470 cm^{-1} is found to originate from opposite vibration of H atom and TaS$_2$ layer against each other. On the other hand, the out-of-plane mode at 339 cm^{-1} is attributed to the breathing-like vibration of top-S–H and lower-S–Ta pairs oppositely. Moreover, similar to A$_u$ mode of symmetric TaS$_2$, the mode having frequency originates from the opposite vibration of Ta-layer and H–S–S layers. The highest frequency nondegenerate mode is found to originate from the top-S and H bond stretching at frequency of 2440 cm^{-1}. As shown in the Raman spectrum given on the right panel of Fig. 3(b), all of the optical phonon modes are found to be Raman active. However, the phonon modes at 321, 470, and 2440 cm^{-1} are calculated to exhibit high Raman activities as compared with other Raman peaks. Apparently, H adsorptions on one of the surface of TaS$_2$ exhibit similar vibrational features with that of FTaS$_2$ with different phonon mode frequencies.

Janus-type single layer of TaS$_2$

As shown in Fig. 4(a), Janus-type single layer of TaS$_2$ is formed by two different surfaces, with one face hydrogenated and the other face fluorinated. The Janus-type single-layer TaS$_2$ belongs to the space group $P6m3$, similar to the other structures mentioned above. Calculated structural parameters are as follows: optimized structure of HTaS$_2$F is a hexagonal structure with lattice parameter ($a = b$) 3.42 Å. The distance between the top and bottom layers is 6.07 Å. The Ta–S bond lengths are 2.43/2.50 Å, whereas that of S–F and S–H are 1.71 and 1.40 Å, respectively. Cohesive energy per atom is 4.58 eV for single layer of Janus TaS$_2$. According to the Bader charge analysis, each Ta atom donates its 1.4 e$^-$ as follows: each S atom receives an average of 0.4 e$^-$, whereas each F atom receives 0.6 e$^-$, and no charge transfer occurs for H atom. As shown in Fig. 5(a), the localization of electrons between H and S shows the covalent bond between them, whereas the bond between F and S is mainly ionic in character. Knowledge of the composition of electronic band structure is crucial for understanding electronic and optical procedures in different electronic and optoelectronic devices. As shown in Fig. 4(c), the electronic band diagram of the Janus type of single-layer TaS$_2$ has a continuous energy distribution at point zero and does not have a gap indicating its metallic character. The graph of PDOS corresponding to the electronic band diagram shows that the highest contribution to the energy bands around the Fermi level originates from the Ta-d orbitals.

As revealed for the single-side functionalized structures of TaS$_2$, the Janus single layer of TaS$_2$ is also found to be dynamically stable. Figure 4(b) shows the phonon band dispersions of Janus single-layer TaS$_2$ exhibiting twelve optical phonon branches. The phonon band gap is found to be
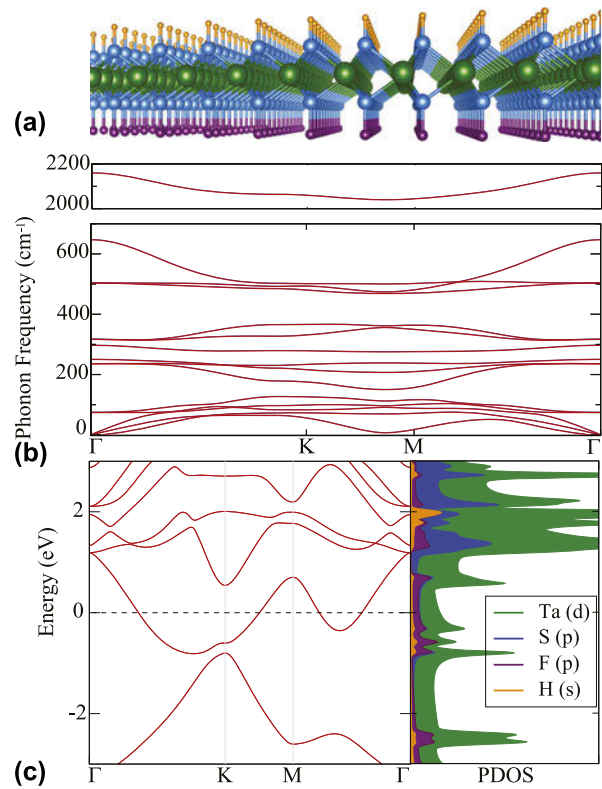

Figure 4: For the single-layer of Janus TaS$_2$; (a) Perspective side view where green, blue, purple, and orange colors represent Ta, S, F, H atoms, respectively. (b) Phonon band dispersions and Raman spectrum. (c) The electronic band structure with the corresponding PDOS. The Fermi level energy is set to 0 eV.
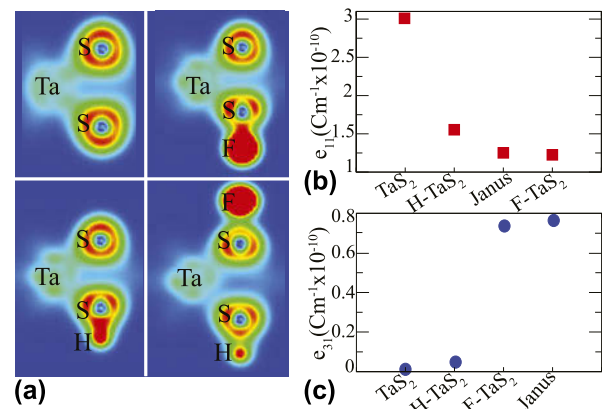

Figure 5: (a) Contour plots of the total charge density ρT in the plane passing through S–Ta–S, S–Ta–S–H, S–Ta–S–F, F–S–Ta–S–H atom, respectively.

27 cm^{-1} which is in between that of FTaS$_2$ and HTaS$_2$. The nondegenerate out-of-plane phonon modes are calculated to have frequencies 250, 297, 647, and 2160 cm^{-1}. The other optical phonon modes which are doubly degenerate in-plane modes have frequencies 74, 236, 317, and 503 cm^{-1}, respectively.

The out-of-plane mode having frequency 250 cm^{-1} is found to originate from the opposite vibration of Ta layer against the whole other atomic layers. Apparently, the mode has similar vibrational character with that of A_u in single-layer TaS$_2$. By contrast, in the mode at a frequency of 297 cm^{-1}, the H–S and F–S pairs vibrate out-of-phase, whereas the Ta layer vibrates in-phase with F–S pair. Because of their nonsymmetric vibrational characters, both of the modes are expected to be Raman inactive. The phonon mode at frequency 647 cm^{-1} is attributed to the out-of-phase vibrations of H and S, and F and S, respectively. By contrast, the highest frequency mode, at 2160 cm^{-1}, originates from the H–S bond stretching. On the other hand, the frequencies of the in-plane phonon modes vary between 74 and 503 cm^{-1}, which indicates that the lateral force constants are weaker than those of the vertical components. The lowest frequency mode arises from the opposite vibrations of F-layer and the top-S–Ta couples, whereas the mode having frequency 236 cm^{-1} originates from the top-S–H couples and the lower S layer against each other. In contrast to those two modes, the mode at 317 cm^{-1} represents the contribution of all atomic layers to the vibration in which H–F–Ta layers vibrate in-phase, whereas they are out-of-phase with the two S-layers. The highest frequency in-plane mode is found to have a frequency of 503 cm^{-1}, which shows the shear-like vibration of top-S and H layers against each other. In addition to the phonon band dispersions, the first-order Raman spectrum of the Janus single layer reveals that all of the optical phonon modes are Raman active. The additional Raman peaks arise from the broken out-of-plane symmetry of the structure. The mode at 236 cm^{-1} has the lowest Raman activity, whereas the phonon mode at 2160 cm^{-1} is the most prominent one. Our findings reveal that in the Janus single layer not only the two surface functionalizations but also the broken symmetry induces distinctive features in the vibrational spectrum.

Mechanical, piezoelectric, and thermal properties

2D materials are elastically characterized by two parameters, in-plane stiffness, C, and Poisson ratio, v. Among 2D ultrathin materials, graphene has the largest in-plane stiffness (330 N/m) [56] due to strong in-plane bonding of C atoms; the in-plane stiffness of TaS$_2$ (104.9) is found to be relatively closer to that of single-layer MoS$_2$ (122 N/m) [56], which is known to be softer than graphene. Hydrogenation and fluorination found to soften single-layer TaS$_2$ with C values are 88.0 and 89.7 N/m, respectively. As the Janus-type structure is constructed, the in-plane Ta–S bonds weaken and the in-plane stiffness decreases to 65.3 N/m, which is almost half of that of bare TaS$_2$. Poisson ratio, the ratio of transverse strain to axial strain, is calculated using the formula $v = C_{12}/C_{11}$. As listed in Table II, Poisson ratio for TaS$_2$, FTaS$_2$, and HTaS$_2$ structures are 0.35, 0.21, and 0.23, respectively. In the case of Janus-type TaS$_2$, Poisson ratio is found to be quite large, 0.47, indicating the larger response to the vertically applied load as compared with other TaS$_2$ structures.

Piezoelectricity is a physical process that occurs in materials owing to the absence of centrosymmetry. Piezoelectric materials generate electric field when an external pressure is applied, and the process is known to be reversible. The relaxed-ion piezoelectric stress coefficients, e_{ij}, is the sum of ionic and electronic contributions, and the corresponding piezoelectric strain constants, d_{ij}, are related to each other through the elastic tensor elements, C_{ij}, as follows:

$$d_{11} = \frac{e_{11}}{C_{11} - C_{12}} \quad , \tag{1}$$

$$d_{31} = \frac{e_{31}}{C_{11} + C_{12}} \quad . \tag{2}$$

As listed in Table II, e_{11} value for bare TaS$_2$ is found to be 3.04×10^{-10} C/m, which is smaller than the reported value for single-layer MoS$_2$ (3.88×10^{-10} C/m) [57]. The single layers of FTaS$_2$ and HTaS$_2$ are found to exhibit much lower e_{11} values, 1.24×10^{-10} and 1.51×10^{-10} C/m, respectively, due to extra charge transfer from Ta atom to adsorbed F or H atoms that weakens the in-plane polarization in the crystal. In addition, e_{11} for the Janus HTaS$_2$F single-layer (1.26×10^{-10} C/m) is found to be closer to that of HTaS$_2$. The broken out-of-plane symmetry in single layers of FTaS$_2$, HTaS$_2$, and HTaS$_2$F creates a net dipole moment along the out-of-plane directions resulting in nonzero e_{31} elements. The calculated values for FTaS$_2$ and HTaS$_2$F are close to each other (0.74×10^{-10} and 0.76×10^{-10} C/m, respectively), whereas it is found to be very small for HTaS$_2$, 0.05×10^{-10} C/m. Apparently, the lack of extra charge transfer between H and S atoms does not add any contribution to the out-of-plane polarization. However, strong electronegativity of F atoms results in high charge depletion and considerably large out-of-plane piezoelectricity.

One important property of a material is its thermal behaviors, which is important for applications in nanoscale devices at finite temperatures. As shown in Fig. 6, all four heat capacity curves increase rapidly in the low temperature regime and asymptotically approach the classical limit of $3Nk_B$, where N and k_B denote the number of atoms and the Boltzmann constant, respectively. It is known that the low temperature behavior of the heat capacity of the 2D crystals is determined by the phonon modes. In bare and functionalized TaS$_2$ structures, the low-temperature thermal excitations take place in acoustic phonon branches and, consequently, the heat capacity is governed by the acoustic phonons. As the heat capacities of single-layer TaS$_2$ structures are compared, it is seen that Janus HTaS$_2$F has the highest heat capacity either at

TABLE II: The calculated parameters for single layers of TaS_2, $FTaS_2$, $HTaS_2$, and $HTaS_2F$ are: work function, Φ; in-plane stiffness, C; the relaxed-ion piezoelectric stress, e_{ij}; the corresponding piezoelectric strain coefficients, d_{ij}; and Poisson ratio, ν.

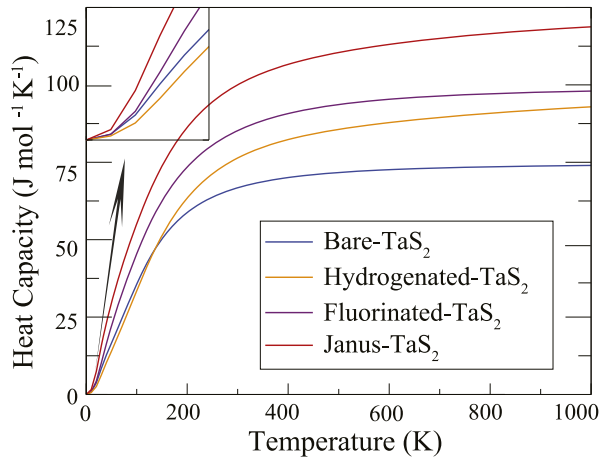|	Φ_{Ta-S} (eV)	Φ_{F-S} (eV)	Φ_{H-S} (eV)	C_{11} (N/m)	C_{12} (N/m)	C (N/m)	e_{11} (C/m × 10^{-10})	e_{31} (C/m × 10^{-10})	d_{11} (pm/V)	d_{31} (pm/V)	ν
TaS_2	5.94	...	...	120.5	42.0	104.9	3.04	0.00	3.87	0.00	0.35
$FTaS_2$	5.39	5.64	...	91.9	19.0	88.0	1.24	0.74	1.70	0.67	0.21
$HTaS_2$	5.50	...	1.86	94.8	21.9	89.7	1.51	0.05	2.07	0.04	0.23
$HTaS_2F$	...	9.35	3.40	84.0	39.6	65.3	1.26	0.76	2.84	0.61	0.47

Figure 6: Heat capacity of single layer of bare-TaS_2, hydrogenated TaS_2, fluorinated TaS_2, and Janus TaS_2.

low or high temperatures. Although at high temperatures single-layer TaS_2 has the lowest heat capacity, the heat capacity of single-layer $HTaS_2$ is the smallest at low temperatures. In addition, at the low temperature limit, the rise of the heat capacity of single-layer TaS_2 structures is not linear with the temperature; instead, the relation is more likely quadratic. As the temperature dependence of the specific heat is $T^{2/n}$ at low temperatures in 2D materials [58], quadratic-like behavior heat capacity of TaS_2 structures reveals the number n to be ≈ 1. Because the frequency of a phonon mode scales with the momentum, q, as $\omega = q^n$, the dispersion of phonon frequency is found to be $\omega = q$ that indicates the contribution of Longitudinal acoustic (LA) and Transverse acoustic (TA) acoustical modes to the low-temperature heat capacity of TaS_2 structures.

Conclusions

In this study, we investigated the structural, vibrational, electronic, and piezoelectric properties of single-layer bare, fluorinated, hydrogenated, and Janus-type TaS_2 by performing state-of-the-art density functional theory calculations. First, it was found that all single-layer TaS_2 crystal structures exhibit hexagonal symmetry with $P6m3$ space groups. Furthermore, we also showed that single-layer TaS_2 can be chemically functionalized by F or H atoms, resulting in dynamically stable

antisymmetric structures. Electronically, our results revealed that single-layer TaS_2 undergoes a metallic to semiconducting behavior via one-side functionalization with either F or H atoms. By contrast, its metallic behavior was predicted to be conserved as it is anti-symmetrically functionalized. The anti-symmetric structure, namely, Janus $HTaS_2F$, has been revealed to possess dynamical stability. The Raman spectrum analysis revealed that breaking the out-of-plane symmetry results in additional Raman active phonon modes in the asymmetric structures of single-layer TaS_2. In addition, the calculated specific heat capacity of TaS_2 structures indicated that in all structures, the longitudinal and transverse acoustical phonon modes contribute to the low-temperature heat capacity. The creation of out-of-plane asymmetry in TaS_2 single layer was shown to result in nonzero piezoelectricity along the out-of-plane direction. The relatively high electronegativity of F atom creates strong out-of-plane piezoelectricity in anti-symmetric TaS_2 structures. Overall, the preserved dynamical stability of TaS_2 under F and H functionalizations makes it a suitable candidate for piezoelectric applications.

Computational methodology

All calculations were performed by using density functional theory (DFT)-based first-principles calculations. The generalized gradient approximation (GGA) in the Perdew–Burke–Ernzerhof (PBE) form [45] was used for the exchange-correlation potential as implemented in the Vienna ab-initio simulation package (VASP) [46, 47]. The van der Waals (vdW) correction to the GGA functional was included by considering the DFT-D2 method of Grimme [48]. Bader [49] technique was used to analyze the charge transfers between the individual atoms in the structures.

For all calculations, a plane-wave basis set with a kinetic energy cutoff of 500 eV was taken. Whereas the convergence criterion of the total force on the atoms in the primitive unitcell was set to 10^{-5} eV/Å, the energy convergence criterion was set to 10^{-6} eV. The pressures on the lattice have been reduced to values less than 1.0 kbar in all directions. A vacuum space of 20 Å was used to eliminate interaction between the adjacent layers. The cohesive energy per formula was calculated by using the formula; $E_{Coh} = [\sum n_{atom} E_{atom} - E_{SL}]/n_{tot}$, where E atom represents the energy of a single isolated atom. E_{SL} is the

Invited Feature Paper

total energy of a single-layer structure, whereas n_{tot} and n_{atom} denote the total number of atoms included in a primitive unitcell and the number of the same type of atoms in the unitcell, respectively. In addition, for the investigation of the dynamical stability of each single-layer, Phonopy code [50] was used. The off-resonant Raman activity of each phonon mode was calculated from the derivative of the dielectric constant with respect to each normal mode at the Γ point of the Brillouin zone (BZ).

Acknowledgments

References

1. K.S. Novoselov, A.K. Geim, S.V. Morozov, D. Jiang, Y. Zhang, S.V. Dubonos, I.V. Grigorieva, and A. Firsov: Electric Field Effect in Atomically Thin Carbon Films. *Science* **306**, 666 (2004).

2. S. Joshi, F. Bischoff, R. Koitz, D. Ecija, K. Seufert, A.P. Seitsonen, J. Hutter, K. Diller, J.I. Urgel, H. Sachdev, J.V. Barth, and W. Auwärter: Control of Molecular Organization and Energy Level Alignment by an Electronically Nanopatterned Boron Nitride Template. *ACS Nano* **8**, 430 (2014).

3. K.K. Kim, A. Hsu, X. Jia, S.M. Kim, Y. Shi, M. Hofmann, D. Nezich, J.F. Rodriguez-Nieva, M. Dresselhaus, T. Palacios, and J. Kong: Synthesis of Monolayer Hexagonal Boron Nitride on Cu Foil Using Chemical Vapor Deposition. *Nano Lett.* **12**, 161 (2012).

4. P. Vogt, P. De Padova, P. Quaresima, J. Avila, E. Frantzeskakis, M.C. Asensio, A. Resta, B. Ealet, and G.L. Lay: Silicene: Compelling Experimental Evidence for Graphenelike Two-Dimensional Silicon. *Phys. Rev. Lett.* **108**, 155501 (2012).

5. S. Cahangirov, M. Topsakal, E. Akturk, H. Sahin, and S. Ciraci: Two- and One-Dimensional Honeycomb Structures of Silicon and Germanium. *Phys. Rev. Lett.* **102**, 236804 (2009).

6. H.L. Zhuang and R.G. Hennig: Electronic structures of single-layer boron pnictides. *Appl. Phys. Lett.* **101**, 153109 (2012).

7. A.K. Geim and I.V. Grigorieva: Van der Waals heterostructures. *Nature* **499**, 419–425 (2013).

8. D.J. Late, B. Liu, J. Luo, A. Yan, H.S.S. Matte, M. Grayson, C.N.R. Rao, and V.P. Dravid: GaS and GaSe Ultrathin Layer Transistors. *Adv. Mater.* **24**, 3549 (2012).

9. D. Jariwala, V.K. Sangwan, L.J. Lauhon, T.J. Marks, and M.C. Hersam: Emerging Device Applications for Semiconducting Two-Dimensional Transition Metal Dichalcogenides. *ACS Nano* **8**, 1102 (2014).

10. C. Tan and H. Zhang: Two-dimensional transition metal dichalcogenide nanosheet-based composites. *Chem. Soc. Rev.* **44**, 2713 (2015).

11. X. Qian, J. Liu, L. Fu, and J. Li: Quantum spin Hall effect in two-dimensional transition metal dichalcogenides. *Science* **346**, 1344 (2014).

12. S.W. Han, H. Kwon, S.K. Kim, S. Ryu, W.S. Yun, D.H. Kim, J.H. Hwang, J.S. Kang, J. Baik, H.J. Shin, and S.C. Hong: Band-gap transition induced by interlayer van der Waals interaction in MoS_2. *Phys. Rev. B* **84**, 045409 (2011).

13. J.K. Ellis, M.J. Lucero, and G.E. Scuseria: The indirect to direct band gap transition in multilayered MoS_2 as predicted by screened hybrid density functional theory. *Appl. Phys. Lett.* **99**, 261908 (2011).

14. D.Y. Qiu, F.H. da Jornada, and S.G. Louie: Optical Spectrum of: Many-Body Effects and Diversity of Exciton States. *Phys. Rev. Lett.* **111**, 216805 (2013).

15. A. Chernikov, T.C. Berkelbach, H.M. Hill, A. Rigosi, Y. Li, O.B. Aslan, D.R. Reichman, M.S. Hybertsen, and T.F. Heinz: Exciton Binding Energy and Nonhydrogenic Rydberg Series in Monolayer WS_2. *Phys. Rev. Lett.* **113**, 076802 (2014).

16. K. He, N. Kumar, L. Zhao, Z. Wang, K.F. Mak, H. Zhao and J. Shan: Tightly bound excitons in monolayer Wse_2. *Phys. Rev. Lett.* **113**, 026803 (2014).

17. A. Ramasubramaniam: Large excitonic effects in monolayers of molybdenum and tungsten dichalcogenides. *Phys. Rev. B* **86**, 115409 (2012).

18. M. Bernardi, M. Palummo, and J.C. Grossman: Extraordinary sunlight absorption and one nanometer thick photovoltaics using two-dimensional monolayer materials. *Nano Lett.* **13**, 3664 (2013).

19. H.R. Gutiérrez, N. Perea-López, A.L. Elías, A. Berkdemir, B. Wang, R. Lv, F. Lòpez-Urías, V.H. Crespi, H. Terrones, and M. Terrones: Extraordinary Room-Temperature Photoluminescence in Triangular WS2 Monolayers. *Nano Lett.* **13**, 3447 (2013).

20. A. Kandemir, B. Akbali, Z. Kahraman, S.V. Badalov, M. Ozcan, F. Iyikanat, and H. Sahin: Structural, electronic and phononic properties of PtSe22: from monolayer to bulk. *Semicond. Sci. Technol.* **33**, 085002 (2018).

21. F. Iyikanat, H. Sahin, R.T. Senger, and F.M. Peeters: Structural Transitions in Monolayer MoS2 by Lithium Adsorption. *J. Phys. Chem. C* **119**, 10709–10715 (2015).

22. K. Wu, E. Torun, H. Sahin, B. Chen, X. Fan, A. Pant, D.P. Wright, T. Aoki, F.M. Peeters, E. Soignard, and S. Tongay: Unusual lattice vibration characteristics in whiskers of the pseudo-one-dimensional titanium trisulfide TiS_3. *Nat. Commun.* **7**, 12952 (2016).

23. A.K. Geremew, S. Rumyantsev, F. Kargar, B. Debnath, A. Nosek, M.A. Bloodgood, M. Bockrath, T.T. Salguero, R.K. Lake, and A.A. Balandin: Bias-Voltage Driven Switching of the Charge-Density-Wave and Normal Metallic Phases in 1TTaS$_2$ Thin-Film Devices. *ACS Nano* **13**, 7231–7240 (2019).

24. N.F. Hinsche and S.K. Tygesen: Electronphonon interaction and transport properties of metallic bulk and monolayer transition metal dichalcogenide TaS$_2$. *2D Mater.* **5**, 015009 (1972).

25. Y. Yu, F. Yang, X.F. Lu, Y.J. Yan, Y-H. Cho, L. Ma, X. Niu, S. Kim, Y-W. Son, D. Feng, D.S. Li, S-W. Cheong, X.H. Chen, and Y. Zhang: Gate-tunable phase transitions in thin flakes of 1T-TaS$_2$. *Nat. Nanotechnol.* **10**, 270–276 (2015).

26. J. Shi, X. Wang, S. Zhang, L. Xiao, Y. Huan, Y. Gong, Z. Zhang, Y. Li, X. Zhou, M. Hong, Q. Fang, Q. Zhang, X. Liu, L. Gu, Z. Liu, and Y. Zhang: Two-dimensional metallic tantalum disulfide as ahydrogen evolution catalyst. *Nat. Commun.* **8**, 958 (2017).

27. R.R. Nair, W. Ren, R. Jalil, I. Riaz, V.G. Kravets, L. Britnell, P. Blake, F. Schedin, A.S. Mayorov, S. Yuan, M. Katsnelson, H-M. Cheng, W. Strupinski, L.G. Bulusheva, A.V. Okotrub, I.V. Grigorieva, A.N. Grigorenko, K.S. Novoselov, and A.K. Geim: Fluorographene: A Two-Dimensional Counterpart of Teflon. *Small* **6**, 2877–2884 (2010).

28. H. Sahin, M. Topsakal, and S. Ciraci: Structures of fluorinated graphene and their signatures. *Phys. Rev. B* **83**, 115432 (2011).

29. M. Yagmurcukardes: Formation of a thin monolayer via fluorination of InSe. *Phys. Rev. B* **100**, 024108 (2019).

30. V. Sreepal, M. Yagmurcukardes, S.K. Vasu, D.J. Kelly, S.F.R. Taylor, V.G. Kravets, Z. Kudrynskyi, Z.D. Kovalyuk, A. Patanè, A.N. Grigorenko, S.J. Haigh, C. Hardacre, L. Eaves, H. Sahin, A.K. Geim, F.M. Peeters, and R.R. Nair: Two-Dimensional Covalent Crystals by Chemical Conversion of Thin van der Waals Materials. **19**, 6475–6481 (2019).

31. J. Wang, S. Chen, X. Quan, and H. Yu: Fluorine-doped carbon nanotubes as an efficient metal-free catalyst for destruction of organic pollutants in catalytic ozonation. *Chemosphere* **190**, 135–143 (2018).

32. J. Zhao, C.R. Cabrera, Z. Xia, and Z. Chen: Singlesided fluorine functionalized graphene: A metalfree electrocatalyst with high efficiency for oxygen reduction reaction. *Carbon* **104**, 56–63 (2016).

33. Y. Li, Z. Zhu, J. Yu, and B. Ding: Carbon Nanotubes Enhanced Fluorinated Polyurethane Macroporous Membranes for Waterproof and Breathable Application. *ACS Appl. Mater. Interfaces* **7**, 13538–13546 (2015).

34. M. Yagmurcukardes, C. Bacaksiz, R.T. Senger, and H. Sahin: Hydrogen-induced structural transition in single-layer ReS$_2$. *2D Mater.* **4**, 035013 (2017).

35. J.O. Sofo, A.S. Caudhari, and G.D. Barber: Graphane: A two-dimensional hydrocarbon. *Phys. Rev. B* **75**, 153401 (2007).

36. M.S. Fuhrer, C.N. Lau, and A.H. MacDonald: Graphene: Materially Better Carbon. *MRS Bull.* **35**, 289–295 (2010).

37. T.O. Wehling, K.S. Novoselov, S.V. Morozov, E.E. Vdovin, M.I. Katsnelson, A.K. Geim, and A.I. Lichtenstein: Molecular Doping of Graphene. *Nano Lett.* **8**, 173–177 (2008).

38. J.T. Robinson, J.S. Burgess, C.E. Junkermeier, S.C. Badescu, T.L. Reinecke, F.K. Perkins, M.K. Zalalutdniov, J.W. Baldwin, J.C. Culbertson, P.E. Sheehan, and E.S. Snow: Properties of Fluorinated Graphene Films. *Nano Lett.* **10**, 3001–3005 (2010).

39. A-Y. Lu, H. Zhu, J. Xiao, C-P. Chuu, Y. Han, M-H. Chiu, C-C. Cheng, C-W. Yang, K-H. Wei, Y. Yang, Y. Wang, D. Sokaras, D. Nordlund, P. Yang, D.A. Muller, M-Y. Chou, X. Zhang, and L-J. Li: Janus monolayers of transition metal dichalcogenides. *Nanotechnol* **12**, 744 (2017).

40. A. Kandemir and H. Sahin: Janus single-layers of In$_2$SSe: A first-principles study. *Phys. Rev. B* **97**, 155410 (2018).

41. J. Zhang, S. Jia, I. Kholmanov, L. Dong, D. Er, W. Chen, H. Guo, Z. Jin, V.B. Shenoy, L. Shi, and J. Lou: Janus Monolayer Transition-Metal Dichalcogenides. *ACS Nano* **11**, 8192–8198 (2017).

42. Y.C. Cheng, Z.Y. Zhu, M. Tahir, and U. Schwingenschlögl: Spin-orbit-induced spin splittings in polar transition metal dichalcogenide monolayers. *Europhys. Lett.* **102**, 57001 (2013).

43. L. Dong, J. Lou, and V.B. Shenoy: Large In-Plane and Vertical Piezoelectricity in Janus Transition Metal Dichalchogenides. *ACS Nano* **11**, 82428248 (2017).

44. Z. Kahraman, A. Kandemir, M. Yagmurcukardes, and H. Sahin: Single-Layer Janus-Type Platinum Dichalcogenides and Their Heterostructures. *J. Phys. Chem. C* **123**, 4549–4557 (2019).

45. J.P. Perdew, K. Burke, and M. Ernzerhof: Generalized Gradient Approximation Made Simple. *Phys. Rev. Lett.* **77**, 3865 (2016).

46. G. Kresse and J. Hafner: Ab initio molecular dynamics for liquid metals. *Phys. Rev. B* **47**, 558 (1993).

47. G. Kresse and J. Furthmüller: Efficient iterative schemes for ab initio total-energy calculations using a plane-wave basis set. *Phys. Rev. B* **54**, 11169 (1996).

48. S. Grimme: Semiempirical GGAtype density functional constructed with a longrange dispersion correction. *J. Comput. Chem.* **27**, 1787–1799 (2006).

49. G. Henkelman, A. Arnaldsson, and H.A. Jonsson: A fast and robust algorithm for Bader decomposition of charge density. *Comput. Mater. Sci.* **36**, 354–360 (2006).

50. A. Togo, F. Oba, and I. Tanaka: First-principles calculations of the ferroelastic transition between rutile-type and CaCl$_2$-type SiO$_2$ at high pressures. *Phys. Rev. B* **78**, 134106 (2008).

51. C. Ataca and S. Ciraci: Functionalization of Single-Layer MoS2 Honeycomb Structures. *J. Phys. Chem. C* **115**, 13303 (2011).

52. D.C. Elias, R.R. Nair, T.M.G. Mohiuddin, S.V. Morozov, P. Blake, M.P. Halsall, A.C. Ferrari, D.W. Boukhvalov, M.I. Katsnelson, A.K. Geim, and K.S. Novoselov: Control of Graphene's Properties by Reversible Hydrogenation: Evidence for Graphane. *Science* **323**, 610–613 (2009).

53. **F. Iyikanat, A. Kandemir, H.D. Ozaydn, R.T. Senger, and H. Sahin**: Hydrogenation-driven phase transition in single-layer TiSe₂. *Nanotechnology* **28**, 495709 (2017).

54. **M. Yagmurcukardes, R.T. Senger, F.M. Peters, and H. Sahin**: Mechanical properties of monolayer GaS and GaSe crystals. *Phys. Rev. B* **94**, 245407 (2016).

55. **M. Yagmurcukardes, C. Sevik, and F.M. Peters**: Electronic, vibrational, elastic, and piezoelectric properties of monolayer Janus MoSTe phases: A first-principles study. *Phys. Rev. B* **100**, 045415 (2019).

56. **H. Sahin**: Structural and phononic characteristics of nitrogenated holey graphene. *Phys. Rev. B* **92**, 085421 (2015).